

Photonic Floquet topological insulators

Mikael C. Rechtsman^{1*}, Julia M. Zeuner^{2*}, Yonatan Plotnik^{1*}, Yaakov Lumer¹, Daniel Podolsky¹, Felix Dreisow², Stefan Nolte², Mordechai Segev¹ & Alexander Szameit²

Topological insulators are a new phase of matter¹, with the striking property that conduction of electrons occurs only on their surfaces^{1–3}. In two dimensions, electrons on the surface of a topological insulator are not scattered despite defects and disorder, providing robustness akin to that of superconductors. Topological insulators are predicted to have wide-ranging applications in fault-tolerant quantum computing and spintronics. Substantial effort has been directed towards realizing topological insulators for electromagnetic waves^{4–13}. One-dimensional systems with topological edge states have been demonstrated, but these states are zero-dimensional and therefore exhibit no transport properties^{11,12,14}. Topological protection of microwaves has been observed using a mechanism similar to the quantum Hall effect¹⁵, by placing a gyromagnetic photonic crystal in an external magnetic field⁵. But because magnetic effects are very weak at optical frequencies, realizing photonic topological insulators with scatter-free edge states requires a fundamentally different mechanism—one that is free of magnetic fields. A number of proposals for photonic topological transport have been put forward recently^{6–10}. One suggested temporal modulation of a photonic crystal, thus breaking time-reversal symmetry and inducing one-way edge states¹⁰. This is in the spirit of the proposed Floquet topological insulators^{16–19}, in which temporal variations in solid-state systems induce topological edge states. Here we propose and experimentally demonstrate a photonic topological insulator free of external fields and with scatter-free edge transport—a photonic lattice exhibiting topologically protected transport of visible light on the lattice edges. Our system is composed of an array of evanescently coupled helical waveguides²⁰ arranged in a graphene-like honeycomb lattice^{21–26}. Paraxial diffraction of light is described by a Schrödinger equation where the propagation coordinate (z) acts as ‘time’²⁷. Thus the helicity of the waveguides breaks z -reversal symmetry as proposed for Floquet topological insulators. This structure results in one-way edge states that are topologically protected from scattering.

Paraxial propagation of light in photonic lattices is described by the Schrödinger-type equation:

$$i\partial_z \psi(x, y, z) = -\frac{1}{2k_0} \nabla^2 \psi(x, y, z) - \frac{k_0 \Delta n(x, y, z)}{n_0} \psi(x, y, z) \quad (1)$$

where $\psi(x, y, z)$ is the electric field envelope function defined by $E(x, y, z) = \psi(x, y, z) \exp(ik_0 z - i\omega t)$; E is the electric field, \mathbf{x} is a unit vector and t is time; the Laplacian, ∇^2 , is restricted to the transverse (x – y) plane; $k_0 = 2\pi n_0/\lambda$ is the wavenumber in the ambient medium; $\omega = 2\pi c/\lambda$ is the optical frequency; and c and λ are respectively the velocity and wavelength of light. Our ambient medium is fused silica with refractive index $n_0 = 1.45$, and $\Delta n(x, y, z)$ is the ‘effective potential’, that is, the deviation from the ambient refractive index. The array is fabricated using the femtosecond laser writing method; each elliptical waveguide has a cross-section with major and minor axis diameters of 11 μm and 4 μm , respectively. The photonic lattice is an array of evanescently-coupled waveguides arranged in a honeycomb structure with nearest-neighbour spacing of 15 μm . The total propagation length (in the z direction) is 10 cm, which corresponds to the wavefunction ψ

of a single waveguide mode completing ~ 20 cycles in phase while propagating from $z = 0$ to $z = 10$ cm. The increase in refractive index associated with the waveguides is $\Delta n = 7 \times 10^{-4}$. The quantum mechanical analogue of equation (1) describes the propagation of a quantum particle that evolves in time—for example, an electron in a solid. The waveguides act like potential wells, similarly to nuclei of atoms in solids. Thus, the propagation of light in the array of helical waveguides as it propagates in the z direction is equivalent to the temporal evolution of an electron as it moves through a two-dimensional lattice with atoms that are rotating in time.

A microscope image of the input facet of the photonic lattice is shown in Fig. 1a, and a diagram of the helical waveguides arranged in a honeycomb lattice is shown in Fig. 1b. The period (or pitch) of the helical waveguides is sufficiently small that a guided mode is adiabatically drawn along with a waveguide as it curves. We therefore transform the coordinates into a reference frame where the waveguides are invariant in the z direction (i.e., straight), namely: $x' = x + R \cos(\Omega z)$, $y' = y + R \sin(\Omega z)$ and $z' = z$, where R is the helix radius and $\Omega = 2\pi/Z$ = $2\pi/1$ cm is the frequency of rotation ($Z = 1$ cm being the period). In the transformed coordinates, the light evolution is described by:

$$i\partial_{z'} \psi' = -\frac{1}{2k_0} (\nabla' + i\mathbf{A}(z'))^2 \psi' - \frac{k_0 R^2 \Omega^2}{2} \psi' - \frac{k_0 \Delta n(x', y')}{n_0} \psi' \quad (2)$$

where $\psi' = \psi(x', y', z')$, and $\mathbf{A}(z') = k_0 R \Omega [\sin(\Omega z'), -\cos(\Omega z'), 0]$ is equivalent to a vector potential associated with a spatially homogeneous electric field of circular polarization. The adiabaticity of the guided modes and the presence of the vector potential yield a coupled mode (tight-binding) equation, via the Peierls substitution¹⁰:

$$i\partial_{z'} \psi_n(z') = \sum_{\langle m \rangle} c e^{i\mathbf{A}(z') \cdot \mathbf{r}_{mn}} \psi_m(z') \quad (3)$$

where the summation is taken over neighbouring waveguides; $\psi_n(z')$ is the amplitude in the n th waveguide, c is the coupling constant between waveguides and \mathbf{r}_{mn} is the displacement between waveguides m and n . Because the right-hand side of equation (3) is z -dependent, there are no static eigenmodes. Rather, the solutions are described using Floquet modes, of the form $\psi_n(z') = \exp(i\beta z') \varphi_n(z')$, where the function $\varphi_n(z')$ is Z -periodic¹⁸. This yields the spectrum of β (the Floquet eigenvalues or ‘quasi-energies’) as a function of the Bloch wavevector, (k_x, k_y) , as well as their associated Floquet eigenmodes. Floquet eigenmodes in the z direction are equivalent to Bloch modes in the x – y plane. Therefore, our input beam (initial wavefunction) excites a superposition of Floquet modes whose population does not change over the course of propagation^{17,18}. The band structure for the case of non-helical waveguides ($R = 0$) is shown in Fig. 1c. The conical intersections between the first and second bands are the ‘Dirac points’²⁸, a feature of graphene that makes it semi-metallic. When the waveguides are made helical ($R > 0$), a bandgap in the Floquet spectrum opens, as shown in Fig. 1d, and the photonic lattice becomes analogous to an insulator—indeed, to a Floquet topological insulator. As we show below, this structure possesses topologically protected edge states.

¹Department of Physics and the Solid State Institute, Technion – Israel Institute of Technology, Haifa 32000, Israel. ²Institute of Applied Physics, Abbe Center of Photonics, Friedrich-Schiller-Universität Jena, Max-Wien-Platz 1, 07743 Jena, Germany.

*These authors contributed equally to this work.

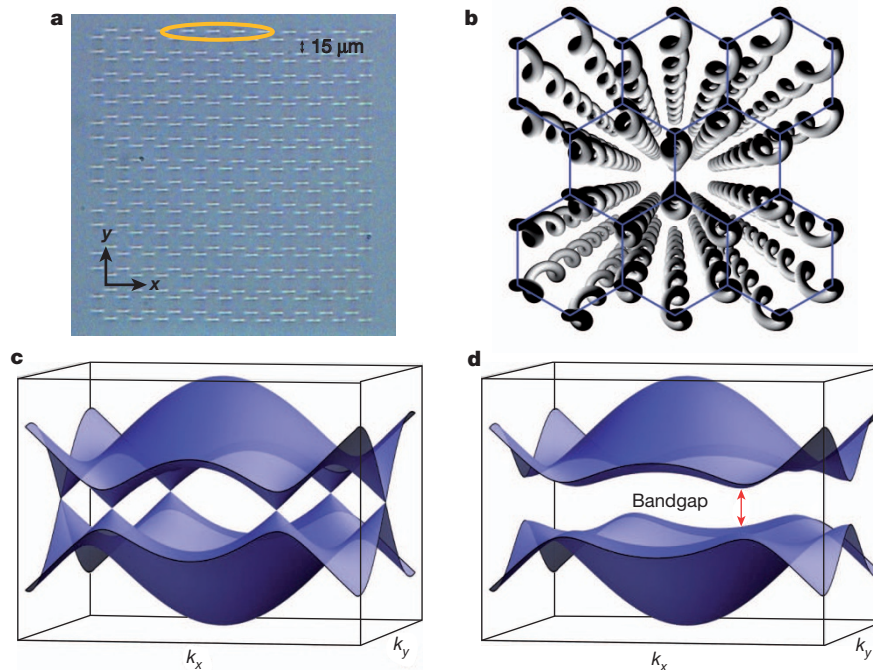


Figure 1 | Geometry and band structure of honeycomb photonic Floquet topological insulator lattice. **a**, Microscope image of the input facet of the photonic lattice, showing honeycomb geometry with 'zig-zag' edge terminations on the top and bottom, and 'armchair' terminations on the left and right sides. Scale bar at top right, 15 μm . The yellow ellipse indicates the position and shape of the input beam to this lattice. **b**, Sketch of the helical waveguides. Their rotation axis is in the z direction, with radius R and period

Z . **c**, Band structure (β versus (k_x, k_y)) for the case of non-helical waveguides comprising a honeycomb lattice ($R = 0$). Note the band crossings at the Dirac point. **d**, Bulk band structure for the photonic topological insulator: helical waveguides with $R = 8 \mu\text{m}$ arranged in a honeycomb lattice. Note the bandgap opening up at the Dirac points (labelled with the red, double-ended arrow), which corresponds to the bandgap in a Floquet topological insulator.

We calculate the edge band structure by using a unit cell that is periodic in the x direction but finite in the y direction, ending with two 'zig-zag' edges (infinite in the x direction). The zig-zag edge is one of three typical edge terminations of the honeycomb lattice; the other two are the 'armchair edge' and the 'bearded edge'. Note that the presence of chiral edge states can be derived using the bulk-edge correspondence principle by calculating the Chern number^{4,5,17,29}. In our sample (see Fig. 1a), the top and bottom edges are zig-zag edges and the right and left edges are armchair edges. The band structure of the zig-zag edge is presented in Fig. 2a for the case where the waveguides are not helical ($R = 0$). There are two sets of states, one per edge. Their dispersion curves are flat and completely coincide (that is, they are degenerate with one another), residing between $k_x = 2\pi/3a$ and $k_x = 4\pi/3a$, occupying one-third of k_x space, where $a = 15\sqrt{3} \mu\text{m}$ is the lattice constant. The Floquet band structure when the lattice is helical with $R = 8 \mu\text{m}$ is shown in Fig. 2b. Here, the edge states are no longer degenerate, but now have opposite slopes. Specifically, the transverse group velocity

(i.e., the group velocity in the $(x-y)$ plane) on the top edge is now directed to the right, and on the bottom edge to the left, corresponding to clockwise circulations. However, there are no edge states whatsoever circulating in the anti-clockwise direction. Hence, the edge states presented in Fig. 2b are the topologically protected edge states of a Floquet topological insulator. The lack of a counter-propagating edge state on a given edge directly implies that any edge-defect (or disorder) cannot backscatter, as there is no backwards-propagating state available into which to scatter, contrary to the case of $R = 0$, where there are multiple states into which scattering is possible. This is the essence of why topological protection occurs. The transverse group velocity (for brevity, we henceforth drop 'transverse') of these edge states has a non-trivial dependence on the helix radius, R . For small R , the group velocity of the edge states increases, but eventually it reaches a maximum and decreases again. Before the group velocity crosses zero, the Chern number is calculated to be -1 (indicating the presence of a clockwise edge state, as seen in Fig. 2b). However, after the group velocity crosses

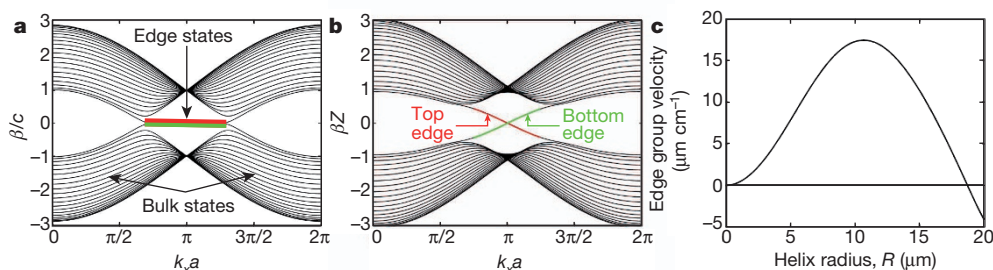


Figure 2 | Dispersion curves of the edge states, highlighting the unique dispersion properties of the topologically protected edge states for helical waveguides in the honeycomb lattice. **a**, Band structure of the edge states on the top and bottom of the array when the waveguides are straight ($R = 0$). The dispersion of both top and bottom edge states (red and green curves) is flat, therefore they have zero group velocity. The bands of the bulk honeycomb lattice

are drawn in black. **b**, Dispersion curves of the edge states in the Floquet topological insulator for helical waveguides with $R = 8 \mu\text{m}$: the band gap is open and the edge states acquire non-zero group velocity. These edge states reside strictly within the bulk band gap of the bulk lattice (drawn in black). **c**, Group velocity (slope of green and red curves) versus helix radius, R , of the helical waveguides comprising the honeycomb lattice. The maximum occurs at $R = 10.3 \mu\text{m}$.

zero—at which point the band gap closes—the Chern number is 2 (indicating the presence of two anti-clockwise edge states, as confirmed by calculations). The R dependence of the group velocity is shown in Fig. 2c, where we plot the group velocity of the topologically protected edge state at $k_x = \pi/a$ versus R . The maximum calculated group velocity is at $R = 10.3 \mu\text{m}$.

To demonstrate these edge states experimentally, we launch a beam with an elliptic profile of wavelength 633 nm such that it is incident on the top row of waveguides in an array with helix radius $R = 8 \mu\text{m}$. The position of the input beam is indicated by the ellipse in Fig. 1a. The light distribution emerging from the output facet is presented in Fig. 3a–d, with the shape and position of the input beam indicated by a yellow ellipse. In Fig. 3a, the beam emerges at the upper-right corner of the lattice, having moved along the upper edge. When we move the position of the input beam horizontally to the right, the output beam moves down along the vertical right edge, as shown in Fig. 3b. The beam emerging from the lattice remains confined to the edge, not spreading into the bulk and without any backscattering. Moving the position of the input beam further rightward makes the output beam move farther down along the side edge, as shown in Fig. 3c and d. Clearly, the input beam has moved along the top edge, encountered the corner, and then continued moving downward along the right edge. We show this behaviour in beam-propagation-method (BPM) simulations³⁰, solving equation (1) (see Supplementary Video 1). The central observation of these experimental results is that the corner (which is in essence a strong defect) does not backscatter light. Indeed, no optical intensity is evident along the top edge at the output facet, after having backscattered from the corner. Furthermore, no scattering into the bulk of the array is observed (owing to the presence of a bulk band-gap). These observations provide strong evidence of topological protection of the edge state.

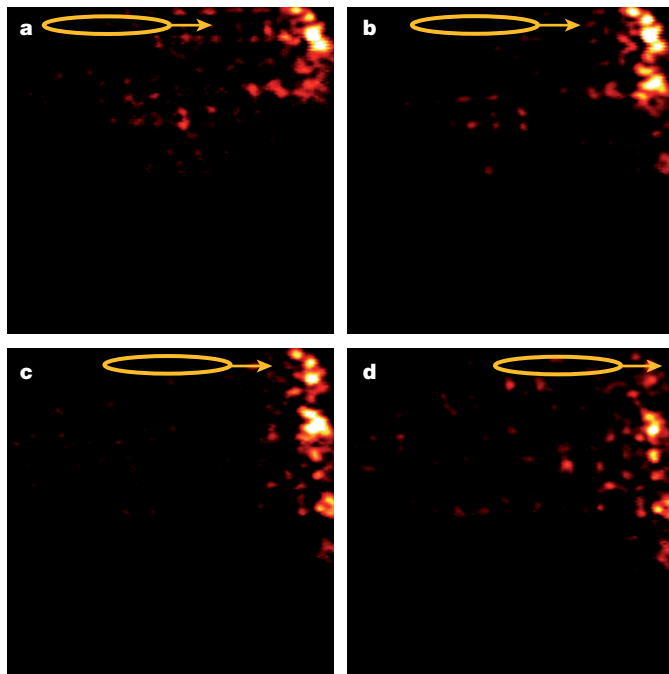


Figure 3 | Light emerging from the output facet of the waveguide array as the input beam is moved rightwards, along the top edge of the waveguide array. The yellow ellipse at the top of each panel shows the position of the input beam (which is at the top of the array, see Fig. 1a), which is moved progressively to the right in a–d. The beam propagates along the top edge of the array (which is in the zig-zag configuration), hits the corner, and clearly moves down the vertical edge (which is in the armchair configuration). Note that the wavepacket shows no evidence of backscattering or bulk scattering due to its impact with the corner of the lattice. This scattering of the edge state is prevented by topological protection.

Further evidence follows from the fact that light stays confined to the side edge of the array as it propagates downwards. This edge is in the armchair geometry, which, for straight waveguides ($R = 0$) does not allow edge confinement at all (that is, no edge states). However, when $R > 0$, edge state dispersion calculations reveal that a confined edge state emerges. This is essential for the topological protection because it prevents transport into the bulk of the lattice.

We now experimentally examine the behaviour of the topological edge states as the helix radius, R , is varied. We find that the group velocity reaches a maximum and then returns to zero as R is increased, in accordance with Fig. 2c. To investigate this, we fabricate a series of honeycomb lattices of helical waveguides with increasing values of R , cut in a triangular shape (Fig. 4a). We first examine light propagation in the lattice with non-helical waveguides (that is, $R = 0$; Fig. 4b). Launching a beam into the waveguide at the upper-left corner of the triangle (circled) excites two types of eigenstates: (1) bulk states extending to the corner, and (2) edge states that meet at the corner. As the light propagates in the array, the excited bulk states lead to some degree of spreading into the bulk (the excitation of these bulk modes can be eliminated by engineering the beam to only overlap with eigenstates confined to the edge). In contrast, the edge states do not spread into the bulk, and, because the edge states are all degenerate (Fig. 2a), they do not cause spreading along the edges either (that is, zero group velocity). Figure 4b shows the intensity at the output facet highlighting this effect: while some light has diffracted into the bulk, the majority remains at the corner waveguide. This is also shown in simulations (where the animation evolves by sweeping through the z coordinate from $z = 0 \text{ cm}$ to $z = 10 \text{ cm}$); see Supplementary Video 2.

When the helical waveguides have clockwise rotation, the edge states are no longer degenerate. In fact, the lattice now has a set of edge states that propagate only clockwise on the circumference of the triangle. Light at the corner no longer remains there, and moves along the edge. Figure 4b–j shows the output facet of the lattice for increasing radius R . For $R = 8 \mu\text{m}$, the wave packet wraps around the corner of the triangle and moves along the opposite edge (Fig. 4f) (the corresponding simulation is shown in Supplementary Video 3; the loss of intensity over the course of propagation is due to bending/radiation losses). Importantly, the light is not backscattered even when it hits the acute corner, owing to the lack of a counter-propagating edge state. This is a key example of topological protection against scattering. For $R = 12 \mu\text{m}$, the wavepacket moves along the edge, but with a slower group velocity. This is consistent with the prediction that the group velocity of the edge state reaches a maximum at $R = 10.3 \mu\text{m}$ and thereafter decreases with increasing radius. The experiments suggest that the maximal group velocity is achieved between $6 \mu\text{m}$ and $10 \mu\text{m}$, while the theoretical result ($10.3 \mu\text{m}$) is well within experimental error, given that this is a prediction from coupled-mode theory. Exact simulations confirm the experimental result.

By $R = 16 \mu\text{m}$, bending losses are large, leading to leakage of optical power into scattering modes (accounting for the large background signal). The bending losses for $R = 4 \mu\text{m}$, $8 \mu\text{m}$, $12 \mu\text{m}$ and $16 \mu\text{m}$ were found to be, respectively, 0.03 dB cm^{-1} , 0.5 dB cm^{-1} , 1.7 dB cm^{-1} and 3 dB cm^{-1} . Recall that each lattice has propagation length $z = 10 \text{ cm}$. The large background signal prevents us from experimenting with larger R , where we would expect two anti-clockwise-propagating edge states, as discussed earlier. As shown in Fig. 4j, the group velocity of the wavepacket approaches zero and therefore the optical power remains at the corner waveguide. These observations clearly demonstrate the presence of one-way edge states on the boundary of the photonic lattice that behave according to theory. Note that for different initial beams—the elliptical beam of Fig. 3, and the single-waveguide excitation of Fig. 4—the topological edge state behaves exactly as the model predicts, providing experimental proof of the existence of the topological edge state.

To demonstrate the z dependence of the wavepacket as it propagates along the edge, we turn to a combination of experimental results and

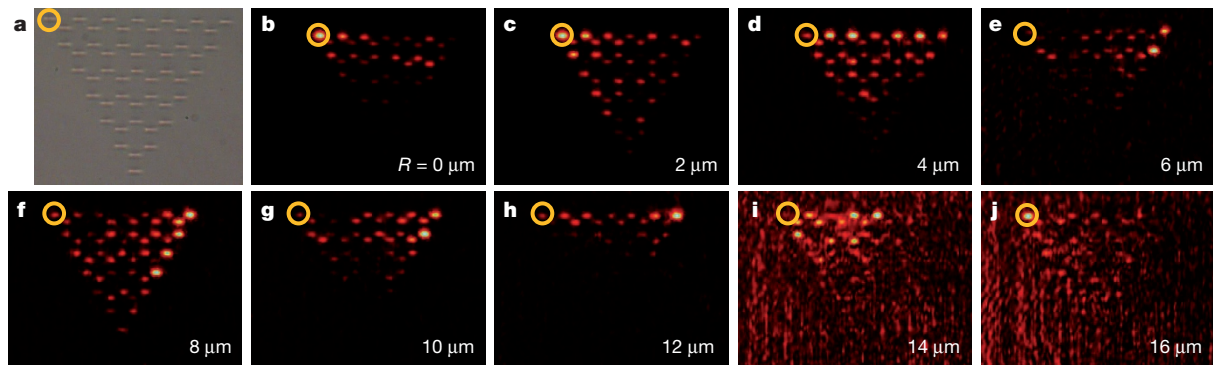


Figure 4 | Experiments highlighting light circulation along the edges of a triangular-shaped lattice of helical waveguides arranged in a honeycomb geometry. **a**, Microscope image of the honeycomb lattice in the triangular configuration. **b–j**, Light emerging from the output facet of the photonic lattice (after 10 cm of propagation) for increasing helix radius, R (given at bottom right of each panel), at wavelength 633 nm. The light is initially launched into the waveguide at the upper-left corner (on the input facet of the array, indicated by a yellow circle). At $R = 0$ (**b**), the initial beam excites a confined defect mode at

the corner. As the radius is increased (**c–j**), light is moving along the edge by virtue of a topological edge mode. It reaches its maximum displacement near $R = 8 \mu\text{m}$ (**f**). The light wraps around the corner of the triangle and is not backscattered at all: this is a clear example of topological protection against scattering. As R is increased further, the light exhibits a decreasing group velocity as a function of R , and finally stops near $R = 16 \mu\text{m}$. The large degree of background noise in **i** and **j** is due to high bending losses of the waveguides as a result of coupling to free-space scattering modes.

simulations of equation (1)³⁰. We examine a lattice with a defect on the edge in the form of a ‘missing’ waveguide (Fig. 5a). Because of topological protection, the wavepacket should simply propagate around the missing waveguide (the defect) without backscattering. An experimental image of the output facet is shown in Fig. 5b (for $R = 8 \mu\text{m}$). The excited waveguide is at the top right, and the edge state propagates clockwise, avoiding the defect, and eventually hitting the next corner. In Fig. 5c–h we show simulations for the optical intensity at $z = 0, 2, 4, 6, 8, 10$ cm, respectively. The wavepacket clearly propagates around the

defect, continuing forward without backscattering. Note that the simulated wavepacket has progressed slightly farther than that in the experiment. This is a result of small uncertainty in the coupling constant, c . Taken together, these data show the progression of topologically protected modes as they travel along the edge.

Photonic Floquet topological insulators have the potential to provide an entirely new platform for probing and understanding topological protection. For example, our photonic lattices have the same geometry as photonic crystal fibres, and thus these systems are likely to exhibit robust topologically protected states. Many interesting open questions are prompted, concerning (for example) the behaviour of entangled photons in a topologically protected system, the effect of interactions on the non-scattering behaviour, or the possibility of simulating photonic Majorana fermions for applications in robust quantum computing. The realization of a photonic Floquet topological insulator in our relatively simple classical system will enable these questions, as well as many others, to be addressed.

Received 17 December 2012; accepted 12 March 2013.

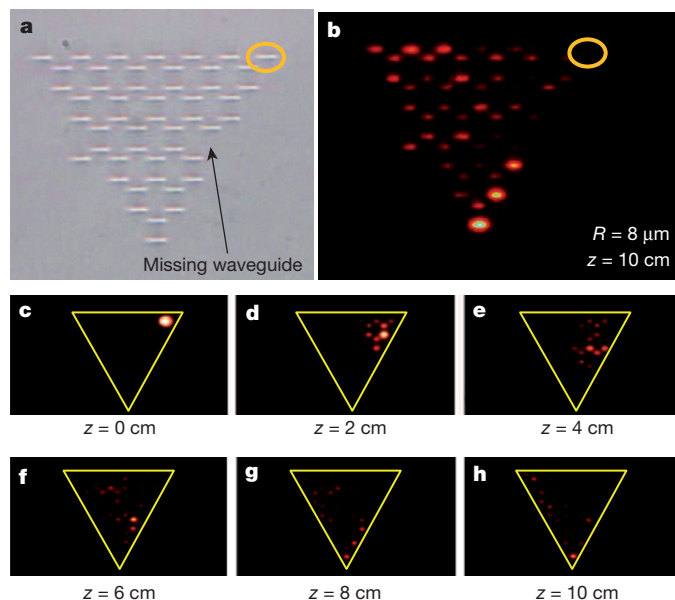


Figure 5 | Experiments and simulations showing topological protection in the presence of a defect. The lattice is triangular-shaped, and the waveguides are helical with $R = 8 \mu\text{m}$. **a**, Microscope image of photonic lattice with a missing waveguide (acting as a defect, arrowed) on the rightmost zig-zag edge. A light beam of $\lambda = 633$ nm is launched into the single waveguide at the upper-right corner (on the far side of the array, surrounded by a yellow circle). **b**, Experimental image of light emerging from the output facet after $z = 10$ cm of propagation, showing no backscattering despite the presence of the defect (a signature of topological protection). **c–h**, Numerical simulations of light propagation through the lattice at various propagation distances (respectively $z = 0$ cm, 2 cm, 4 cm, 6 cm, 8 cm and 10 cm). After minimal bulk scattering, the light propagates along the edge, encounters the defect, propagates around it, and continues past it without scattering, in agreement with **b**.

1. Kane, C. L. & Mele, E. J. Quantum spin Hall effect in graphene. *Phys. Rev. Lett.* **95**, 226801 (2005).
2. König, M. *et al.* Quantum spin Hall insulator state in HgTe quantum wells. *Science* **318**, 766–770 (2007).
3. Hsieh, D. *et al.* A topological Dirac insulator in a quantum spin Hall phase. *Nature* **452**, 970–974 (2008).
4. Haldane, F. D. M. & Raghu, S. Possible realization of directional optical waveguides in photonic crystals with broken time-reversal symmetry. *Phys. Rev. Lett.* **100**, 013904 (2008).
5. Wang, Z., Chong, Y., Joannopoulos, J. D. & Soljacic, M. Observation of unidirectional backscattering-immune topological electromagnetic states. *Nature* **461**, 772–775 (2009).
6. Koch, J., Houck, A. A., Hur, K. L. & Girvin, S. M. Time-reversal-symmetry breaking in circuit-QED-based photon lattices. *Phys. Rev. A* **82**, 043811 (2010).
7. Umucalilar, R. O. & Carusotto, I. Artificial gauge field for photons in coupled cavity arrays. *Phys. Rev. A* **84**, 043804 (2011).
8. Hafezi, M., Demler, E. A., Lukin, M. D. & Taylor, J. M. Robust optical delay lines with topological protection. *Nature Phys.* **7**, 907–912 (2011).
9. Khanikaev, A. B. *et al.* Photonic topological insulators. *Nature Mater.* **12**, 233–239 (2012).
10. Fang, K., Yu, Z. & Fan, S. Realizing effective magnetic field for photons by controlling the phase of dynamic modulation. *Nature Photon.* **6**, 782–787 (2012).
11. Kraus, Y. E., Lahini, Y., Ringel, Z., Verbin, M. & Zilberberg, O. Topological states and adiabatic pumping in quasicrystals. *Phys. Rev. Lett.* **109**, 106402 (2012).
12. Kitagawa, T. *et al.* Observation of topologically protected bound states in photonic quantum walks. *Nature Commun.* **3**, 882 (2012).
13. Lu, L., Joannopoulos, J. D. & Soljacic, M. Waveguiding at the edge of a three-dimensional photonic crystal. *Phys. Rev. Lett.* **108**, 243901 (2012).
14. Malkova, N., Hromada, I., Wang, X., Bryant, G. & Chen, Z. Observation of optical Shockley-like surface states in photonic superlattices. *Opt. Lett.* **34**, 1633–1635 (2009).

15. Klitzing, K. v., Dorda, G. & Pepper, M. New method for high-accuracy determination of the fine-structure constant based on quantized Hall resistance. *Phys. Rev. Lett.* **45**, 494–497 (1980).
16. Oka, T. & Aoki, H. Photovoltaic Hall effect in graphene. *Phys. Rev. B* **79**, 081406 (2009).
17. Kitagawa, T., Berg, E., Rudner, M. & Demler, E. Topological characterization of periodically driven quantum systems. *Phys. Rev. B* **82**, 235114 (2010).
18. Lindner, N. H., Refael, G. & Galitski, V. Floquet topological insulator in semiconductor quantum wells. *Nature Phys.* **7**, 490–495 (2011).
19. Gu, Z., Fertig, H. A., Arovas, D. P. & Auerbach, A. Floquet spectrum and transport through an irradiated graphene ribbon. *Phys. Rev. Lett.* **107**, 216601 (2011).
20. Szameit, A. & Nolte, S. Discrete optics in femtosecond-laser-written photonic structures. *J. Phys. B* **43**, 163001 (2010).
21. Peleg, O. *et al.* Conical diffraction and gap solitons in honeycomb photonic lattices. *Phys. Rev. Lett.* **98**, 103901 (2007).
22. Bahat-Treidel, O., Peleg, O. & Segev, M. Symmetry breaking in honeycomb photonic lattices. *Opt. Lett.* **33**, 2251–2253 (2008).
23. Ablowitz, M. J., Nixon, S. D. & Zhu, Y. Conical diffraction in honeycomb lattices. *Phys. Rev. A* **79**, 053830 (2009).
24. Fefferman, C. L. & Weinstein, M. I. Honeycomb lattice potentials and Dirac points. *J. Am. Math. Soc.* **25**, 1169–1220 (2012).
25. Rechtsman, M. C. *et al.* Strain-induced pseudomagnetic field and photonic Landau levels in dielectric structures. *Nature Photon.* **7**, 153–158 (2013).
26. Crespi, A., Corrielli, G., Della Valle, G., Osellame, R. & Longhi, S. Dynamic band collapse in photonic graphene. *New J. Phys.* **15**, 013012 (2013).
27. Lederer, F. *et al.* Discrete solitons in optics. *Phys. Rep.* **463**, 1–126 (2008).
28. Novoselov, K. S. *et al.* Two-dimensional gas of massless Dirac fermions in graphene. *Nature* **438**, 197–200 (2005).
29. Zak, J. Berry's phase for energy bands in solids. *Phys. Rev. Lett.* **62**, 2747–2750 (1989).
30. Kawano, K. & Kitoh, T. *Introduction to Optical Waveguide Analysis: Solving Maxwell's Equation and the Schrödinger Equation* (Wiley & Sons, 2001).

Supplementary Information is available in the online version of the paper.

Acknowledgements M.C.R. is grateful to the Azrieli Foundation for the Azrieli fellowship while at the Technion. M.S. acknowledges the support of the Israel Science Foundation, the USA-Israel Binational Science Foundation, and an Advanced Grant from the European Research Council. A.S. thanks the German Ministry of Education and Research (Center for Innovation Competence program, grant 03Z1HN31) and the Thuringian Ministry for Education, Science and Culture (Research group Spacetime, grant 11027-514) for support. The authors thank S. Raghu and T. Pereg-Barnea for discussions.

Author Contributions The idea was conceived by Y.P. and M.C.R. The theory was investigated by M.C.R. and Y.P. The fabrication was carried out by J.M.Z. The experiments were carried out by M.C.R., Y.P. and J.M.Z. All authors contributed considerably.

Author Information Reprints and permissions information is available at www.nature.com/reprints. The authors declare no competing financial interests. Readers are welcome to comment on the online version of the paper. Correspondence and requests for materials should be addressed to M.C.R. (mcrworld@gmail.com) and Y.P. (yonatanplotnik@gmail.com).